

# On line-of-sight navigation for deep-space applications: A performance analysis

Stefano Casini<sup>a,b,\*</sup>, Angelo Cervone<sup>a</sup>, Bert Monna<sup>b,c,1</sup>, Eberhard Gill<sup>a</sup>

<sup>a</sup> Delft University of Technology, Kluyverweg 1, Delft 2629 HS, The Netherlands

<sup>b</sup> AAC Hyperion, Vlinderweg 2, Delft 2623 AX, The Netherlands

<sup>c</sup> Phosphoenix, Meibergdreef 5, Amsterdam 1105 AZ, The Netherlands

Received 30 March 2022; received in revised form 30 November 2022; accepted 7 December 2022

Available online 15 December 2022

## Abstract

Line-of-Sight (LoS) navigation is an optical navigation technique that exploits the direction to visible celestial bodies, obtained from an onboard imaging system, to estimate the position and velocity of a spacecraft. The directions are fed to an estimation filter, where they are matched with the actual position of the observed bodies, retrieved from onboard stored ephemerides. As LoS navigation represents a really promising option for the next-generation deep-space spacecraft, the objective of this work is to provide new insights into the performance. First, the information matrix is analyzed to show the influence of the geometry between the spacecraft and the observed planet (s). Then, a Monte Carlo approach is used to investigate the influence of measurement error (ranging from 0.1 to 100 arcsec), and tracking frequency (ranging from four observations per day to one observation every two days). The effect on navigation performance is quantified by two indicators. The first is the 3D position and velocity Root-Mean-Square-Errors, computed once the estimation is considered to be steady-state. The second is the convergence time, which quantifies the required time for the estimation to reach the steady-state behaviour. The simulation is based on a set of four planets, which do not follow the common heliocentric dynamics but rotate around the Sun with the same (distance-independent) angular velocity of the spacecraft. This approach allows the separation of scenario-dependent behaviours from navigation intrinsic properties, as the same relative geometry between observer and observed objects is maintained during the whole simulation. The results provide a useful guide for the next-generation autonomous navigation system, for both the definition of hardware requirements and the design of an appropriate navigation strategy. Considerations are then applied to Near-Earth Asteroid fly-by mission scenarios for the definition of the navigation strategy and hardware requirements. It is shown the importance of relative angles between the spacecraft and the planets. In the single-planet observation scenario, when the angle between the position vectors of the spacecraft and planet approaches a null value, the estimation error decreases. In the double-planets observation scenario, when the separation angle between the two LoS directions gets close to 90°, the estimation error decreases. The main influence on the performance is driven by the measurement error, which with current technologies is shown to be able to provide a position error in the order of a few hundred kilometers, while with a lower measurement error (0.1 arcsec) it would be possible to have a position error below 100 km. Finally, it is demonstrated that tracking frequency plays a secondary role in the performance, and only influences tangibly the convergence time.

© 2022 COSPAR. Published by Elsevier B.V. This is an open access article under the CC BY license (<http://creativecommons.org/licenses/by/4.0/>).

**Keywords:** Autonomous navigation; Star-trackers; Deep-space CubeSats

\* Corresponding author at: Delft University of Technology, Kluyverweg 1, Delft 2629 HS, The Netherlands.

E-mail addresses: [s.casini@tudelft.nl](mailto:s.casini@tudelft.nl) (S. Casini), [a.cervone@tudelft.nl](mailto:a.cervone@tudelft.nl) (A. Cervone), [bert.monna@aac-clydespace.com](mailto:bert.monna@aac-clydespace.com) (B. Monna), [e.k.a.gill@tudelft.nl](mailto:e.k.a.gill@tudelft.nl) (E. Gill).

<sup>1</sup> The co-author Bert Monna is not anymore employed at AAC Hyperion (affiliation b), but he was at the time of the paper analysis and writing.

## 1. Introduction

Nowadays demand for space exploration is increasing, both for scientific and commercial purposes. Sustainable use of space is gaining popularity, and, because of that, a higher autonomy level of spacecraft is particularly desirable, as it can cut down the cost associated with the space mission, but also decrease the need for the ground segment. Moreover, from a more general perspective, the exploitation of autonomous techniques can be also linked to a reduction of onboard instrumentation need, which is translated into a lower-mass payload for the launcher, or eventually to larger volume and mass allocated for scientific instrumentation (Casini et al., 2021).

Concerning autonomous navigation, several techniques have been proposed through the years (Turan et al., 2022a). Depending on the mission scenario, distinctions can be highlighted between relative navigation techniques, as around a planet (Enright et al., 2018), the Moon (Franzese et al., 2018) or a small body (Frauenholz et al., 2008; Pellacani et al., 2019), or absolute navigation, as around Lagrangian points in cislunar space (Turan et al., 2022b) or during a deep-space cruise around the Sun. This paper focuses on a particular type of optical navigation, namely LoS (Line-of-Sight) navigation, which is particularly suitable for deep-space cruising applications. The technique is based on the observation of directions to visible celestial bodies, that are obtained onboard using optical instrumentation, either cameras or star-trackers. Indeed, this technique appears to be a viable option for autonomous deep-space CubeSats, as cameras and star trackers, usually carried onboard, can be exploited for navigation, without increasing mass and volume. Moreover, the combination of CubeSat and autonomous navigation can have an impact on Near-Earth Asteroids (NEAs) missions, as the exploration of a large number of targets can benefit from a cost reduction per mission, and an increased level of autonomy.

As of today, no space mission has exploited only LoS navigation to estimate the state of an interplanetary cruising spacecraft, although SMART-1 carried onboard an experiment (Marini et al., 2002). Moreover, it is currently gaining popularity for miniaturized spacecraft, in-fact the stand-alone CubeSat M-ARGO is expected to carry onboard an experiment to test its applicability (Franzese et al., 2021). From a theoretical perspective, the technique has been proposed using a batch estimation technique in Vasile et al. (2002), where the exploitation of a general CCD image acquisition system is mentioned. In Mortari and Conway (2017) a least squares and a weighted least squares method were presented to estimate the Cartesian state of an interplanetary spacecraft, generating an initial orbit determination guess, and mentioning for the first time the applicability of star-trackers. In Karimi and Mortari (2015), the first orbit determination solution is used to initiate a sequential filtering approach. In

Franzese and Topputo (2019) and Machuca et al. (2019), LoS navigation is finally proposed for deep-space CubeSat applications, while the same authors in Franzese and Topputo (2020) propose an analytical approach to select the best pair of visible planets to be observed. In Andreis et al. (2022), an onboard algorithm is developed and tested with a Raspberry Pi. Moreover, in Dahir et al. (2019), the observation of Jupiter and its moons is used both to estimate the state and to reconstruct the onboard timing knowledge.

To complete the set of feasibility assessments available in the literature, it is necessary to expand the set of analyses aimed to characterize the intrinsic LoS navigation properties. In particular, there is still a need to investigate the impact on the navigation performance of two design parameters, namely LoS measurement errors and tracking frequency. Despite their importance for mission design, in literature, their influence is not sufficiently treated. They are necessary to derive hardware requirements for component selection and to define a suitable navigation strategy. For these reasons, this paper is aimed to investigate this technique, through an analysis of factors impacting its performance. However, this is done using a novel approach. In previous works, realistic scenarios were simulated, based on the actual positions of some selected planets during a specific time interval, which in combination with a specific spacecraft orbit, do not provide completely general conclusions. To overcome the dependency on the scenario, a set of four planets is simulated, with different dynamical characteristics from the actual Solar system planets. With this set of planets, a sensitivity analysis on the geometry and on characterizing parameters (LoS measurement error and tracking frequency) is carried out. The results define the expected performance ranges, also as a function of geometric parameters, which are useful both for understanding the general principles of LoS navigation, and for the definition of optimal navigation solutions in realistic mission scenarios.

This work is then intended to serve as a driver for the design of the next-generation autonomous LoS navigation systems, both for the hardware selection and for the navigation strategy plan. Two NEAs fly-by test cases are then defined to show how the derived general considerations apply to realistic mission scenarios.

The paper is organized as follows: in Section 2, the analysis framework is presented. First, LoS navigation is briefly introduced together with the Kalman filter formulation used for this study, and then the simulation approach and the parameters under investigation are presented; in Section 3, a semi-analytical approach is exploited to investigate the influence of the geometry on the navigation performance; in Section 4, the results of the Monte Carlo analysis are shown. In Section 5, two realistic test cases are analyzed in connection with the results reported in Sections 3 and 4. Finally, conclusions are drawn, highlighting what is required to improve and use this technique for space exploration.

## 2. Analysis framework

The next subsections explain the various items related to the analysis. First LoS navigation is introduced. Then, the simulation approach is described, highlighting the dynamics characteristics. Later, the Extended Kalman Filter (EKF) formulation is presented, followed by the definition of the performance indicators and the analyzed parameters.

### 2.1. Line-of-sight navigation

LoS navigation is a technique based on the observation of one or more visible celestial bodies (either planets, moons, or small bodies). Directions to bodies are obtained with an onboard camera (or star-tracker) and are fed to the navigation filter, where they are processed together with the ephemerides of the observed objects (stored onboard). The filter processes this information together with the spacecraft dynamics, and estimates the state (e.g. position and velocity in a heliocentric frame) of the spacecraft. Both observation and estimation phases can be performed autonomously onboard.

The problem's geometry is sketched in Fig. 1. The dephasing angle  $\alpha$  is defined as the angular separation between the position vector of the spacecraft  $\vec{r}$  and the position vector of the observed planet  $\vec{r}_{1,2}$ . The separation angle  $\beta$  is identified as the angular separation between the two LoS vectors  $\vec{r}_{p1}$  and  $\vec{r}_{p2}$  centred in the spacecraft position.

The observation of multiple bodies can occur simultaneously if multiple imagers are available onboard, or asynchronously, either if only one camera can collect the image, or if slew manoeuvres are required to centre the target in the FoV (Field-of-View). For the following analysis, simultaneous imaging will be considered.

### 2.2. Simulation approach

This work aims to provide the reader with new insights into the influence of some parameters on LoS navigation performance. The following analysis is based on a new sim-

ulation approach, to generalize as much as possible the conclusions. Since LoS navigation is strongly reliant on the geometry (and geometry variation) of the problem, the simulation of realistic mission scenarios, characterized by the observation of specific planets, in a specific time frame, from a specific spacecraft orbit, does not allow to dive easily into the intrinsic characteristics of this technique but only allows to assess the applicability to a particular test case. To draw general conclusions, a large set of realistic scenarios should be simulated, adding both complexities due to the various parameters that play a role, and significantly increasing the computation time. Besides this, a clear definition of the steady-state behaviour of the estimation would not be clear, as the geometry variation through the simulation time frame always generates oscillation in the solution. To overcome these problems, the approach consists in simulating a set of four planets, that, despite their actual position in space, maintain the same angular separation with the spacecraft throughout the whole simulation. This is done by forcing their orbital speed to be equal to the spacecraft one. The results of this approach can then be interpreted as the asymptotic behaviour of the solution for a given geometry. The attention is focused on the actual parameters under analysis, as all the others (including geometry) are fixed. This would not be possible for a realistic scenario simulation, as the constantly changing relative geometry would impact the results. Moreover, as it is shown in Section 3, this approach allows a very simplified definition of the information matrix, that is analyzed to draw conclusions on the geometry.

Four planets have been simulated, all of them orbiting around the Sun in a circular orbit in the Ecliptical plane. Their heliocentric radii are respectively 0.4, 0.8, 1.8, and 5.2 AU. These values have been selected to cover four different ranges of planetary distances, which are connected to NEAs region missions. In this paper, the four planets will be referred to as P1 (0.4 AU), P2 (0.8 AU), P3 (1.8 AU), and P4 (5.2 AU).

For the analysis, the spacecraft's orbit is assumed circular and heliocentric, in the Ecliptical plane, with a radius of 1 AU. Again, this has been chosen to simulate a possible NEAs region mission. The selection of a circular orbit is useful to have a symmetric simulation for the analysis of the results, but it is not a limitation of the applicability of the technique to only circular orbits. Actual interplanetary cruise trajectories are not necessarily circular, however, the impact of the trajectory's eccentricity on the navigation performance is currently not investigated, leaving space for further analysis.

With these orbits (spacecraft and planets), the 3D problem becomes 2D. However, this is still compliant with actual mission scenarios, where the relative inclination of the orbits is small (close to  $0^\circ$ ), as NEAs are usually encountered in the proximity of their ascending or descending nodal passages to avoid expensive change-of-plane manoeuvres. Fig. 2 shows a 3D representation of the orbit of each object.

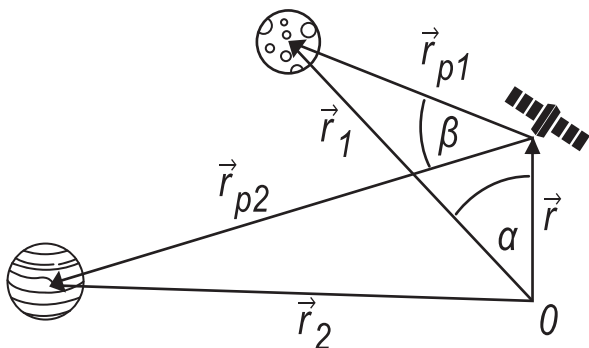


Fig. 1. Two-dimensional sketch of the geometry.

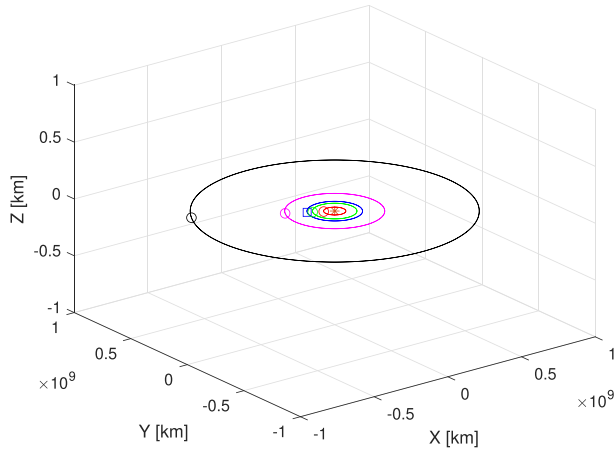


Fig. 2. Visual representation of the spacecraft orbit (blue), and planets orbit in a heliocentric frame.

The angular separation choice between the planets involved in the simulation is presented in Section 4, after the geometry analysis, to justify the selection.

The length of a simulation has been set to 730 days, because it corresponds to two full revolutions of the spacecraft around the Sun, and because a large number of ballistic transfers to NEAs have a shorter Time-of-Flight (ToF).

For the semi-analytical approach and for the sensitivity analysis a 2-body problem dynamics has been implemented:

$$\ddot{\vec{r}} = -\mu_{Sun} \frac{\vec{r}}{r^3} \quad (1)$$

where  $\vec{r}$  is the heliocentric position vector of the spacecraft and  $\mu_{Sun}$  is the solar gravitational parameter. For the semi-analytical approach, it will be shown how the 2-body problem dynamics, in combination with the circularity of the orbits, will lead to a simplified analytical formulation. Moreover, in the sensitivity analysis, the simulation model will allow again to focus attention on the intrinsic characteristics.

On the other hand, the propagation of the trajectories in Section 5 for the realistic scenarios, is based on a higher-fidelity model, composed of the 2-body problem model with the addition of planetary gravitational disturbances (until Saturn), and the Solar Radiation Pressure (SRP), which can be expressed as:

$$\ddot{\vec{r}} = -\mu_{Sun} \frac{\vec{r}}{r^3} + \sum_{k=1}^6 \mu_k \frac{\vec{r}_{pk}}{r_{pk}^3} - \sum_{k=1}^6 \mu_k \frac{\vec{r}_k}{r_k^3} + \vec{a}_{SRP} \quad (2)$$

where  $\mu_k$  are the gravitational parameters of the planets,  $\vec{r}_{pk}$  are the vectors pointing from the spacecraft to the planets,  $\vec{r}_k$  are the heliocentric position vector of the planets, and the SRP is modelled as cannonball (Jean et al., 2019):

$$\vec{a}_{SRP} = \frac{2P_{SRP}}{B} \vec{r} \quad (3)$$

where  $\vec{a}_{SRP}$  is the SRP acceleration aligned with the spacecraft position vector,  $P_{SRP}$  is the pressure exerted on the

spacecraft by the solar radiation, and  $B$  is the mass-to-area ratio of the spacecraft. Respectively they can be computed as:

$$P_{SRP} = \frac{P_0}{c} \left( \frac{R_0}{r} \right)^2 \quad (4)$$

$$B = \frac{m}{A} \quad (5)$$

where  $P_0$  is the solar flux at 1 AU (1367 W/m<sup>2</sup>),  $c$  the speed of light (2.998e08 m/s),  $R_0$  is the Sun-Earth mean distance,  $r$  is the spacecraft-Sun distance,  $m$  is the spacecraft mass, and  $A$  is the spacecraft surface exposed to the SRP, assuming a unitary reflectivity coefficient.

Concerning the simulation, a Monte Carlo approach has been chosen. Each scenario is simulated 200 times, and then the results are presented as the mean value of certain performance indicators (Section 2.5). Each Monte Carlo trial is characterized by a different state initial guess and a different set of observations. Both are computed by adding Gaussian noise (with a certain standard deviation) respectively on top of the actual initial state and the simulated measurements.

### 2.3. Navigation filter

For this application and analysis, a sequential estimation technique has been preferred over a batch approach. During the cruise, real-time operations are not necessary, so a batch approach would be possible. However, as this analysis is carried out bearing in mind its applicability to autonomous deep-space CubeSat, the use of a sequential algorithm is preferred, as a smaller amount of data needs to be stored on-board, and because a constant update of the state estimation allows eventual manoeuvres and operations.

An Extended Kalman Filter formulation has been derived for the problem (Tapley et al., 2004). The state to be estimated is the spacecraft six-dimensional Cartesian state expressed in a heliocentric frame:

$$\vec{X} = \begin{bmatrix} x \\ y \\ z \\ v_x \\ v_y \\ v_z \end{bmatrix} \quad (6)$$

The measurements fed to the EKF are the directions to one or more planets, expressed in terms of azimuth  $\theta$  and elevation  $\phi$  with respect to the observer (e.g. the spacecraft):

$$\vec{Y} = \begin{bmatrix} \theta \\ \phi \end{bmatrix} \quad (7)$$

Directions to planets are expressed in the same heliocentric frame as:



$$\hat{r}_{pk} = \frac{\vec{r}_k - \vec{r}}{|\vec{r}_k - \vec{r}|} = \begin{bmatrix} x_{los,k} \\ y_{los,k} \\ z_{los,k} \end{bmatrix} \quad (8)$$

where  $\vec{r}_k$  is the heliocentric planet position vector. The spacecraft attitude is considered known (in Section 4.1 it is taken into account to define the LoS measurement error range). General EKF equations for the state dynamics and the observation can be expressed as:

$$\vec{X} = f(\vec{X}(t), \vec{u}(t)) \quad (9)$$

$$\vec{Y} = h(\vec{X}(t), \vec{u}(t)) = \begin{bmatrix} \arctan\left(\frac{y_{los,k}}{x_{los,k}}\right) \\ \arcsin(z_{los,k}) \end{bmatrix} \quad (10)$$

where  $\vec{u}$  is the control vector (not implemented in this analysis, as ballistic trajectories are considered). Vector  $\vec{X}$  contains the time-derivatives of the state vector, and it is expressed as a function  $f$  of both state and control vectors, which in the Monte Carlo analysis is based on Eq. (1), while later in the realistic mission scenario analysis is based on a reduced version of Eq. (2).  $\vec{Y}$  is the computed measurements vector (for each observed body), and it is expressed as a function  $h$  of both state and control vectors.

Bold characters in the next equations indicate matrices. The state is propagated within the filter by solving the differential Eq. (1), while the covariance matrix is propagated as:

$$\bar{\mathbf{P}}_k = \Phi^T(t_k, t_{k-1}) \hat{\mathbf{P}}_{k-1} \Phi(t_k, t_{k-1}) + \mathbf{Q} \quad (11)$$

where  $\Phi(t_k, t_{k-1})$  is the state transition matrix and  $\mathbf{Q}$  is the process noise matrix:

$$\mathbf{Q} = \begin{bmatrix} 10^{-12} & 0 & 0 & 0 & 0 & 0 \\ 0 & 10^{-12} & 0 & 0 & 0 & 0 \\ 0 & 0 & 10^{-12} & 0 & 0 & 0 \\ 0 & 0 & 0 & 10^{-10} & 0 & 0 \\ 0 & 0 & 0 & 0 & 10^{-10} & 0 \\ 0 & 0 & 0 & 0 & 0 & 10^{-10} \end{bmatrix} \quad (12)$$

whose diagonal values have been preliminarily tuned considering a high-fidelity propagator for the trajectory, and a 2-body problem propagator in the EKF. While the position elements can be kept small without influencing significantly the performance, the velocity entries require some additional attention. Analysing various 1 AU orbits in different time epochs suggested that a value between  $10^{-9}$  and  $10^{-10}$  allows the estimation error to be kept within the  $3\sigma$  boundaries. So for the following analyses, it has been rounded down to  $10^{-10}$ , considering that the dynamics is perfectly modelled in the filter. Similarly, for the realistic mission scenarios of Section 5, the largest disturbances are modelled in the EKF propagator, so small values are appropriate. Accurate tuning of the  $\mathbf{Q}$  matrix depends on the time propagation interval: the larger the time interval,

the larger the elements of the matrix. In this paper, various tracking frequencies are analyzed, but the  $\mathbf{Q}$  is kept constant because formal tuning is not performed and it is left for further analysis. Nevertheless, the results are not significantly impacted. Furthermore, following the approach reported in Carpenter and D'Souza (2018), the elements of  $\mathbf{Q}$  relative to two tracking frequencies of this analysis would differ by less than an order of magnitude.

The state transition matrix is computed at each time interval by integrating:

$$\dot{\Phi}(t) = \mathbf{F}\Phi(t) \quad (13)$$

where  $\mathbf{F}$  is the Jacobian of the state, and in the 2-body problem formulation can be expressed as:

$$\mathbf{F} = \begin{bmatrix} 0 & 0 & 0 & 1 & 0 & 0 \\ 0 & 0 & 0 & 0 & 1 & 0 \\ 0 & 0 & 0 & 0 & 0 & 1 \\ -\frac{\mu_s}{r^3} \left(1 - \frac{3y^2}{r^2}\right) & 3\mu_s \frac{x}{r^5} & 3\mu_s \frac{yz}{r^5} & 0 & 0 & 0 \\ 3\mu_s \frac{xy}{r^5} & -\frac{\mu_s}{r^3} \left(1 - \frac{3x^2}{r^2}\right) & 3\mu_s \frac{yz}{r^5} & 0 & 0 & 0 \\ 3\mu_s \frac{xz}{r^5} & 3\mu_s \frac{yz}{r^5} & -\frac{\mu_s}{r^3} \left(1 - \frac{3z^2}{r^2}\right) & 0 & 0 & 0 \end{bmatrix} \quad (14)$$

The state vector and covariance matrix update can be then expressed as:

$$\vec{\hat{X}}_k = \vec{\bar{X}}_k + \mathbf{K}_k (\vec{Y}_k - \vec{\bar{Y}}_k) \quad (15)$$

$$\hat{\mathbf{P}}_k = (\mathbf{I} - \mathbf{K}_k \mathbf{H}_k) \bar{\mathbf{P}}_k \quad (16)$$

where  $\vec{\bar{X}}_k$  is the propagated state vector,  $\vec{\hat{X}}_k$  is the updated state vector,  $\vec{Y}_k$  is the measurements vector,  $\vec{\bar{Y}}_k$  is the computed measurements vector,  $\bar{\mathbf{P}}_k$  is the propagated covariance matrix,  $\hat{\mathbf{P}}_k$  is the updated covariance matrix. Respectively, the observation matrix  $\mathbf{H}_k$  and the Kalman gain matrix  $\mathbf{K}_k$  can be expressed as:

$$\mathbf{H}_k = \begin{bmatrix} \frac{y_{los,1}}{r_{los,1}^2} & -\frac{x_{los,1}}{r_{los,1}^2} & 0 & 0 & 0 & 0 \\ \frac{x_{los,1} z_{los,1}}{r_{los,1}^3 \sqrt{1 - \frac{z_{los,1}^2}{r_{los,1}^2}}} & \frac{y_{los,1} z_{los,1}}{r_{los,1}^3 \sqrt{1 - \frac{z_{los,1}^2}{r_{los,1}^2}}} & \frac{z_{los,1}^2 - r_{los,1}^2}{r_{los,1}^3 \sqrt{1 - \frac{z_{los,1}^2}{r_{los,1}^2}}} & 0 & 0 & 0 \\ \frac{y_{los,2}}{r_{los,2}^2} & -\frac{x_{los,2}}{r_{los,2}^2} & 0 & 0 & 0 & 0 \\ \frac{x_{los,2} z_{los,2}}{r_{los,2}^3 \sqrt{1 - \frac{z_{los,2}^2}{r_{los,2}^2}}} & \frac{y_{los,2} z_{los,2}}{r_{los,2}^3 \sqrt{1 - \frac{z_{los,2}^2}{r_{los,2}^2}}} & \frac{z_{los,2}^2 - r_{los,2}^2}{r_{los,2}^3 \sqrt{1 - \frac{z_{los,2}^2}{r_{los,2}^2}}} & 0 & 0 & 0 \end{bmatrix} \quad (17)$$

$$\mathbf{K}_k = \bar{\mathbf{P}}_k \mathbf{H}_k^T (\mathbf{H}_k \bar{\mathbf{P}}_k \mathbf{H}_k^T + \mathbf{R}_k)^{-1} \quad (18)$$

where  $\mathbf{R}_k$  is the observation covariance matrix, assumed constant in this analysis:

$$\mathbf{R}_k = \begin{bmatrix} \sigma_{los1}^2 & 0 & 0 & 0 \\ 0 & \sigma_{los1}^2 & 0 & 0 \\ 0 & 0 & \sigma_{los2}^2 & 0 \\ 0 & 0 & 0 & \sigma_{los2}^2 \end{bmatrix} \quad (19)$$

The observation matrix defined in Eq. (17) corresponds to the double-planets observation scenario, while for the single-planet observation case the matrix reduces the first two rows.

In realistic applications, light-time delay and velocity aberration corrections are needed. The first refers to the fact that light needs a certain amount of time to travel from the body under observation to the spacecraft. This amount of time, namely light-time delay, has to be computed onboard to access the ephemerides at the correct time, which can be also influenced by the onboard timing knowledge. The second is an aberration effect dependent on the relative tangential velocity of the observer (e.g. the spacecraft) with respect to the observed object (e.g. the planet). This effect produces a shift in the position of the object observed by the camera/star-tracker. Both can be easily taken into account within the EKF. Light-time delay can be corrected by iterating the ephemerides access time, as a function of the computed distance observer-body. Velocity aberration can be corrected by estimating algebraically the angular shift (Mortari and Conway, 2017). In this paper, they are taken into account only for the realistic scenario simulations (Section 5), as for the artificial planets approach they would just add complexity to the general case, without bringing interesting insights.

#### 2.4. Performance indicators

Two indicators of the performance of this navigation technique are used within this work. One is the 3D Root-Mean-Square-Error (3D-RMSE, or simply RMSE) of both position and velocity computed over the last half year, when, as it will be shown later, the steady-state has been reached. The other quantifies the amount of time needed to reach a steady-state behaviour of the filter, and it is referred to as convergence time. There is no unique way of defining it, so, in this work, we define a custom criterion to quantify whether the solution has reached steady-state behaviour or not. For each scenario, the mean position 3D-RMSE previously defined is set as the threshold. Then, the average position error evolution is computed, and when the error goes below the threshold, the solution is considered to be steady-state, and the convergence time is recorded. Fig. 3 provides an insight into the behaviour of the position RMSE for a test case (the same conclusions can be drawn for other test cases). As can be noticed, after an initial large RMSE, the curves tend to flatten when the steady-state is approaching. Moreover, the definition of this convergence time criterion is particularly suitable for this sensitivity analysis. Since a variable error in the measurements results in a variable steady-state RMSE (as it

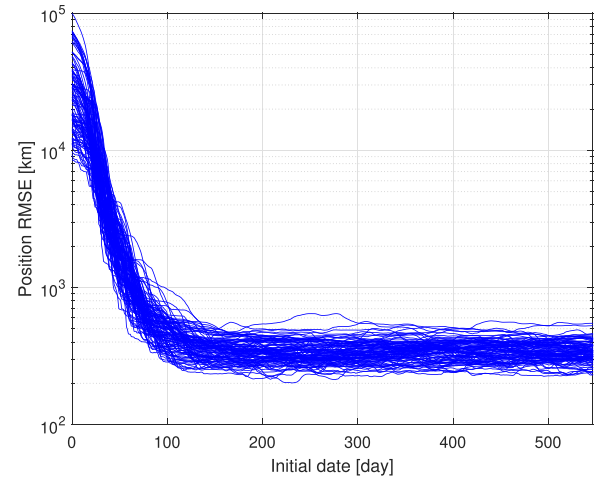


Fig. 3. Position RMSE computed over a time interval of half year, as a function of the initial date of the considered time interval. The scenario is a single tracking planet (P3), with a de-phasing angle equal to  $0^\circ$ . The observation error is 1 arcsec. Tracking frequency is 1 obs/day, and initial position and velocity errors are respectively  $10^5$  km and 0.1 km/s.

will be shown later), the definition of a unique threshold quantifying whether the error has converged or not is reductive. With this approach, each test case has its relative threshold for the definition of steady-state achievement.

#### 2.5. Parameters under analysis

The purpose of this work is to show the influence of two design parameters on navigation performance.

The first is the LoS measurement error. It represents the angular error of the measured direction to the observed body, that is fed to the filter. This value in practical applications especially depends on the attitude determination performance (driven by the star trackers characteristics), on the image processing to compute the centre of the observed body, and on the observation scenario (e.g. observed body, illumination condition, distance from the observer). Then, in addition to those, systematic errors, such as mounting offset, can be considered. For the simulation, Gaussian noise is added on top of the computed azimuth and elevation. The noise standard deviation  $\sigma_{los}$  ranges across four orders of magnitude, exponentially from 0.1 arcsec up to 100 arcsec. Current commercial-off-the-shelf star trackers for small satellites offer an attitude knowledge from a few arcsec up to some tens of arcsec (Casini et al., 2021). However, usually, these values are driven by onboard algorithms that have to ensure low estimation error and at the same time sufficient speed for real-time applications (e.g. pointing, data transmission, de-tumbling etc.). In deep-space cruising applications, speed performance can be partially sacrificed to reach lower error in the estimation. For this reason, a 0.1 arcsec error is also investigated, as it is desirable for the near future.

The second important parameter, whose influence is explored in this work, is the so-called tracking frequency.

It quantifies the time interval between two subsequent observations fed to the filter. This parameter is tunable according to the navigation strategy, in compliance with the operations and power requirements. It is important to define whether a higher frequency of observations determines an improvement in the solution both in a global and in a local perspective. Respectively, four tracking frequencies have been selected: one observation every two days, one per day, two per day, and four per day.

### 3. Semi-analytical geometry analysis

This technique is highly dependent on the geometrical conditions, especially the de-phasing and separation angles, and the distances between the objects. To quantify the effect on the performance of these two parameters it is possible to analyze the information matrix, defined as:

$$\mathbf{\Lambda} = \sum_{k=1}^n \mathbf{\Phi}^T(t_k, t_0) \mathbf{H}_k^T \mathbf{W} \mathbf{H}_k \mathbf{\Phi}(t_k, t_0) \quad (20)$$

where  $\mathbf{H}_k$  is the previously defined observation matrix computed at time  $t_k$ ,  $\mathbf{\Phi}(t_k, t_0)$  is the state-transition matrix, and  $\mathbf{W}$  is the weight matrix, inverse of  $\mathbf{R}$ . The inverse of  $\mathbf{\Lambda}$  is the covariance matrix  $\mathbf{P}$ , whose eigenvalues roots represent the axis of the error ellipsoid in its principal frame, and are used in this analysis to compare the performance of different geometries.

Since in this problem  $\mathbf{W}$  is a constant diagonal matrix (whose elements are assumed to have the same value), it can be taken out of the sum, and the matrix that will be computed and inverted for the analysis is:

$$\tilde{\mathbf{\Lambda}} = \sum_{k=1}^n \mathbf{\Phi}^T(t_k, t_0) \mathbf{H}_k^T \mathbf{H}_k \mathbf{\Phi}(t_k, t_0) \quad (21)$$

which is based exclusively on the geometry of the problem. This matrix can be computed for the whole simulation length (assuming a tracking frequency of one observation per day), and then the eigenvalues of its inverse can be calculated. As already remarked, the problem in a realistic application is almost 2D, so it will be further assumed in this analysis, leading to a four-components state vector. For a circular 2D orbital problem, the state transition matrix can be expressed as:

$$\mathbf{\Phi}(t_k, t_0) = \begin{bmatrix} \cos(n\Delta t) & 0 & \frac{\sin(n\Delta t)}{n} & 0 \\ 0 & \cos(n\Delta t) & 0 & \frac{\sin(n\Delta t)}{n} \\ -n \sin(n\Delta t) & 0 & \cos(n\Delta t) & 0 \\ 0 & -n \sin(n\Delta t) & 0 & \cos(n\Delta t) \end{bmatrix} \quad (22)$$

where  $n$  is the mean motion of the spacecraft and  $\Delta t = t_k - t_0$ . As the problem is 2D, the elevation angle is null, so the only observable is the azimuth. Then, as the separation angle among the objects is forced to be constant through the simulation, the observation matrix can be expressed as:

$$\mathbf{H}_k = \begin{bmatrix} \frac{r_1 \sin(\alpha_1 + n\Delta t) - r \sin(n\Delta t)}{r_{p1}^2} & -\frac{r_1 \cos(\alpha_1 + n\Delta t) - r \cos(n\Delta t)}{r_{p1}^2} & 0 & 0 \\ \frac{r_2 \sin(\alpha_2 + n\Delta t) - r \sin(n\Delta t)}{r_{p2}^2} & -\frac{r_2 \cos(\alpha_2 + n\Delta t) - r \cos(n\Delta t)}{r_{p2}^2} & 0 & 0 \end{bmatrix} \quad (23)$$

where  $\alpha_1$  and  $\alpha_2$  are the de-phasing angles with planets 1 and 2,  $r_1$  and  $r_2$  are the planets heliocentric radii,  $r$  is the spacecraft heliocentric radius, and  $r_{p1}$  and  $r_{p2}$  are the spacecraft-planets distances. This matrix holds for the two-bodies observation scenario, while it reduces to the only first row in case of single-planet tracking case.

The inversion of  $\tilde{\mathbf{\Lambda}}$  is the core of this analysis, however, as it has been shown in Ma et al. (2016), the single-planet tracking case is not fully observable. This leads to instabilities when it comes to invert  $\tilde{\mathbf{\Lambda}}$ , so it has been defined:

$$J = \frac{1}{\text{trace}(\tilde{\mathbf{\Lambda}}_{UL})} \quad (24)$$

which is lower than the trace of  $\mathbf{P}$  (or the sum of its eigenvalues) (Ma et al., 2016), but can still be used to quantify when a geometry is more favourable than another. In particular, this analysis is performed on the 2x2 upper-left partition of  $\tilde{\mathbf{\Lambda}}$ , here defined  $\tilde{\mathbf{\Lambda}}_{UL}$ , to focus on the position estimation (although similar conclusions can be drawn for the velocity). In Fig. 4,  $J$  is reported as a function of the observed planet's semi-major axis and the de-phasing angle with the observer spacecraft. The lower its value, the most favourable the geometry to exploit line-of-sight navigation. As expected, the best tracking conditions for the single-planet tracking scenario are for planets whose position vector is aligned to the position vector of the spacecraft, and that are as close as possible to the observer

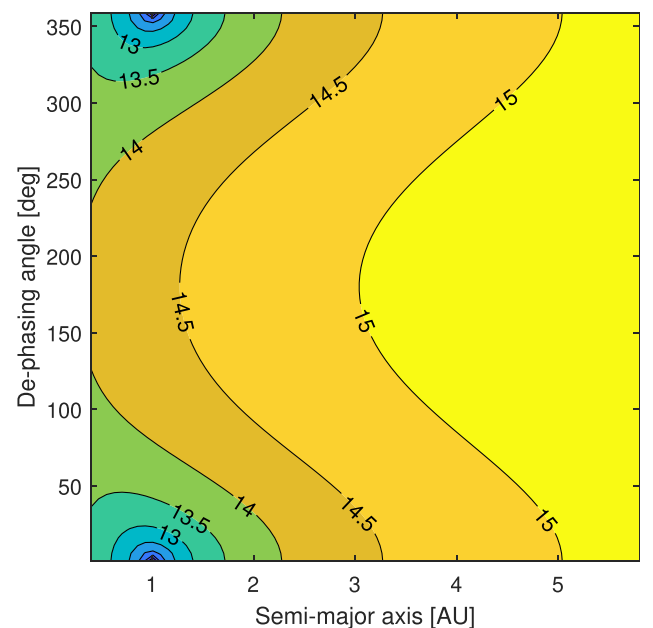


Fig. 4.  $\text{Log}_{10}(J)$  as a function of the planet semi-major axis and the de-phasing angle for the single planet tracking scenario.

(in this case orbiting on a 1AU semi-major axis). This optimal observation scenario is however very difficult to achieve in real missions, as objects with a lower semi-major axis than the spacecraft cannot be observed at low de-phasing angles due to the Sun illumination.

Moreover, the results show how, for a 1AU orbit, the observation of planets with a lower semi-major axis produces better estimates, despite the fixed relative geometry. So, in realistic scenarios, where the geometry is not fixed, the better estimate derived from the observation of inner planets is not only linked to a quicker measurement change, which is usually beneficial for EKF, but it is also connected to this intrinsic property of the technique.

On the other hand, the double-planets tracking case is fully observable, the inverse of  $\tilde{\Lambda}$  can be easily computed, and then the sum of the eigenvalues of  $\mathbf{P}_{UL}$ , denoted as  $\lambda_P$ , can be used to quantify the impact on the geometry. Differently from the single-planet tracking scenario, this case is characterized by four varying parameters: the two semi-major axes and the two de-phasing angles. Then, to show results, two parameters need to be fixed, showing the influence of the other two. For this reason, three cases have been considered: observation of P1-P2, P2-P3, and P3-P4. Figs. 5–7 show respectively the results for the three cases. The larger error (represented by a high value in the plots) corresponds to separation angles close to either  $0^\circ$  or  $180^\circ$ , for all the scenarios. In the plots, it can be noticed how there are wide regions in which LoS navigation can provide good performance, while only in a restricted number of scenarios the geometry is not favourable to achieve low estimation error.

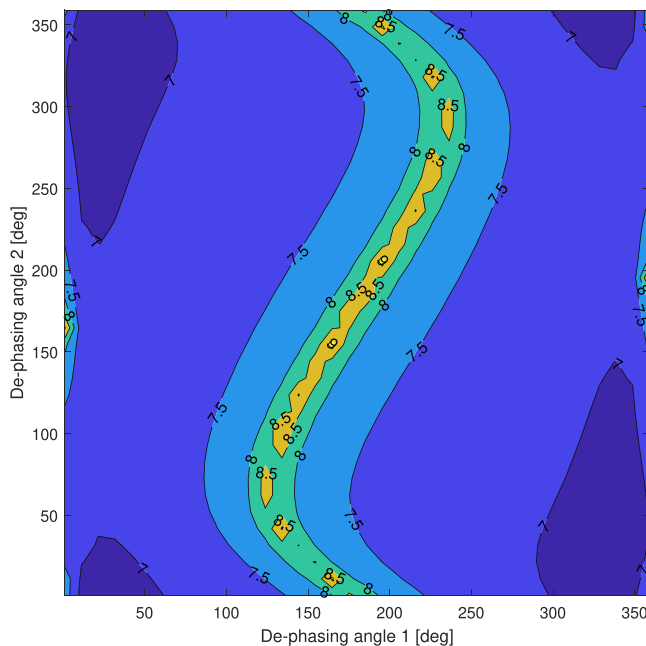


Fig. 5.  $\text{Log}_{10}(\lambda_P)$  as a function of the de-phasing angles of P1 and P2.

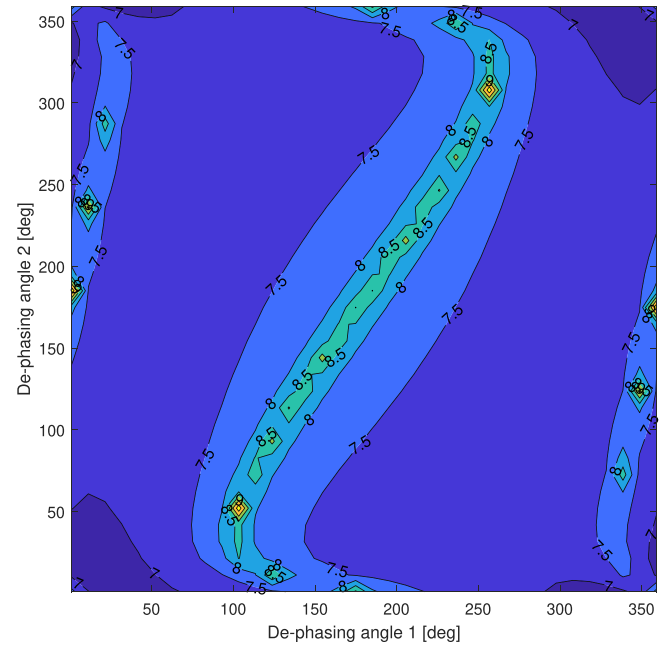


Fig. 6.  $\text{Log}_{10}(\lambda_P)$  as a function of the de-phasing angles of P2 and P3.

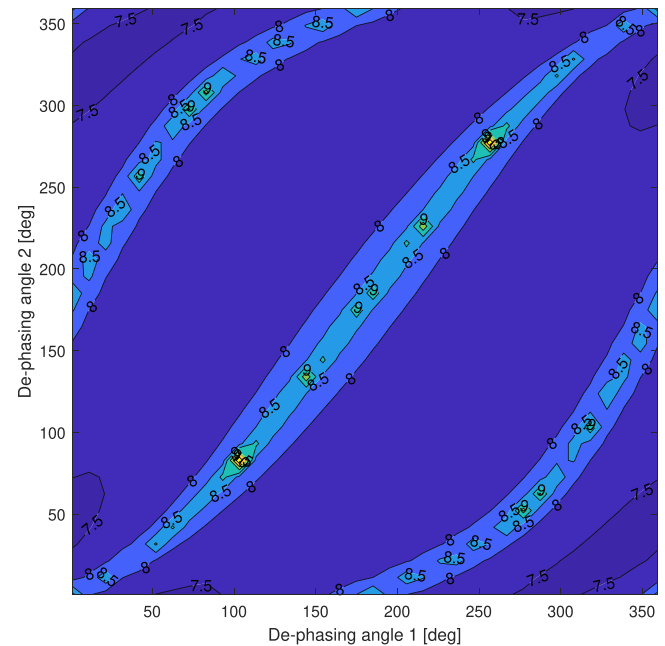


Fig. 7.  $\text{Log}_{10}(\lambda_P)$  as a function of the de-phasing angles of P3 and P4.

#### 4. Sensitivity analysis

The next subsections are devoted to the results of the sensitivity analysis on the LoS measurement error and tracking frequency. First, the focus is given to the RMSE, then the convergence time is analyzed.

LoS measurement error analysis is intended to show the effect of different noise levels in the measurements. The tracking frequency is kept constant to one observation per hour, while the initial error on the state is sampled



respectively with a standard deviation of  $10^5$  km for the position and 0.1 km/s for the velocity. The initial position dispersion is chosen as large for two main reasons: first, it allows showing the potential of LoS navigation to reduce the error even with poor initial conditions; secondly, as it is shown later in the manuscript, in only one test case the position RMSE is larger than  $10^5$  km, so it allows a fair comparison between test cases. The initial velocity dispersion is chosen to maintain approximately the same ratio between the order of magnitude of position and velocity for a 1 AU orbit.

The tracking frequency analysis is aimed to investigate the impact of the number of observations per given time interval. For that, the LoS measurement error is kept constant at 1 arcsec, while the initial position and velocity dispersion is assumed again respectively  $10^5$  km for the position and 0.1 km/s for the velocity.

#### 4.1. Position and velocity RMSE

First, the analysis is performed for the single-planet scenario. Following the considerations reported in Section 3, each planet tracking is simulated both for a de-phasing angle  $\alpha = 0^\circ$ , and for  $\alpha = 90^\circ$ . The first corresponds usually to a lower error scenario in terms of RMSE, while the second represents a larger error scenario.

The results are reported in Figs. 8 and 9. Plots show how the steady state RMSE, both for position and velocity, scales up with the LoS measurement error. For the lower  $\sigma_{los}$ , the RMSE ranges respectively from  $\sim 70$  km to  $\sim 3199$  km for the position, and from  $\sim 0.03$  m/s to  $\sim 0.62$  m/s for the velocity. On the other hand, for the larger  $\sigma_{los}$ , the position RMSE ranges from  $\sim 2231$  km to  $\sim 246110$  km, while the velocity RMSE from  $\sim 0.44$  m/s to  $\sim 47.9$  m/s.

For the two planets observation scenario, eight combinations of planets, de-phasing angle, and separation angle are considered. As it is shown in Section 3, the optimal condition is for a de-phasing angle close to  $0^\circ$  and a separation

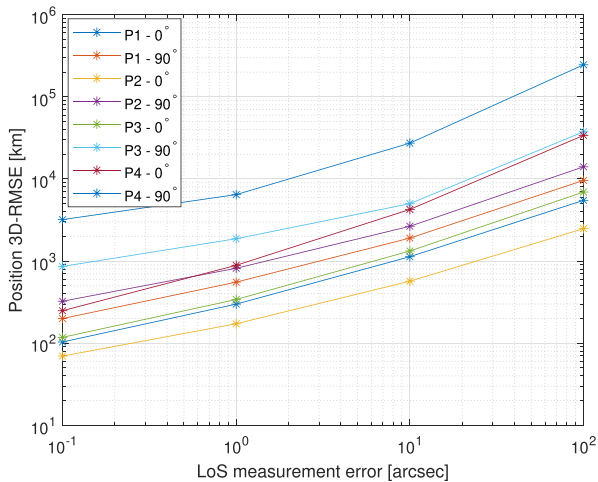


Fig. 8. 3D position steady state RMSE as a function of the LoS standard deviation. Angles in the legend refer to the de-phasing angle.

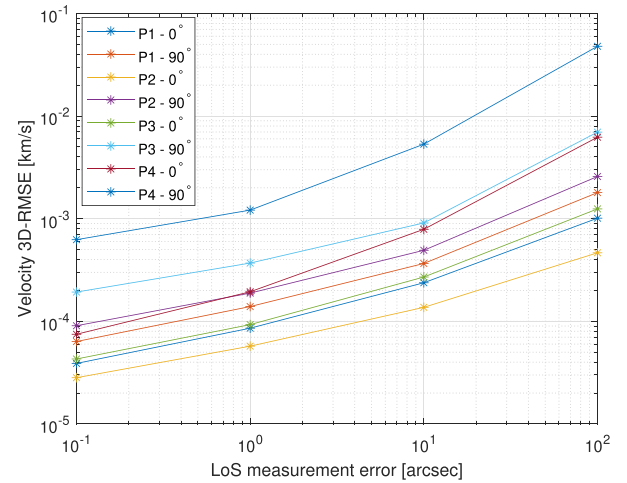


Fig. 9. 3D velocity steady state RMSE as a function of the LoS standard deviation. Angles in the legend refer to the de-phasing angle.

angle close to  $90^\circ$ , but for inner planets, it is not always possible to achieve it. For all combinations, the pair's inner planet is placed in an orbit with de-phasing angle  $0^\circ$ . Then the pair P1-P2 is considered with separation angle  $50^\circ$ , which is almost the maximum permitted by the geometry. For comparison, the other two pairs, P1-P3 and P1-P4, are considered with the same separation angle. For the remaining five combinations, the separation angle is set to  $90^\circ$ .

Similar conclusions to the single-planet tracking scenario can be drawn. The impact on the RMSE is presented in Tables 1 and 2, where respectively the mean RMSE of position and velocity are reported for each scenario, together with the standard deviation. Again, there is a quite significant influence on the performance of the observation error, resulting in a position RMSE in the range  $\sim 25$ – $90$  km in the lower error scenario, and in the range  $\sim 2000$ – $7000$  km in the larger error case. For the velocity RMSE, the ranges are respectively  $\sim 0.026$ – $0.41$  m/s and  $\sim 0.4$ – $1.3$  m/s. Despite the apparent large difference between the position and velocity RMSE (highlighted also in the single-planet observation case), these results are in line with the order of magnitude of the problem, since the position vector components are in the order of  $\sim 10^8$  km, while the velocity ones are in the order of some tens of km/s.

Moreover, it is noteworthy to highlight how the tracking of two planets, rather than one only, produces a systematic and notable performance increase. This can be noticed especially comparing the single-planet case  $P4 - 90^\circ$  with the double-planets case  $P2, P4 - 90^\circ$ , as the position RMSE of the former with an observation error of 0.1 arcsec ( $\sim 3199$  km) is larger than the position RMSE of the latter with an observation error of 100 arcsec ( $\sim 2508$  km).

#### 4.2. Convergence time

This subsection is intended to show the results in terms of convergence time. The goal is to show how quickly the

Table 1

Position mean and standard deviation RMSE [km] per scenario (two planets observation).

Scenario	0.1 arcsec	1 arcsec	10 arcsec	100 arcsec
P1,P2 - 50°	25.87 (2.60)	142.26 (21.04)	664.45 (133.23)	3548.90 (1017.52)
P1,P3 - 50°	37.28 (4.18)	215.27 (40.57)	1020.27 (228.39)	4664.17 (1596.13)
P1,P4 - 50°	90.98 (19.28)	309.321 (45.09)	1078.14 (234.51)	5389.70 (1497.96)
P1,P3 - 90°	39.81 (5.56)	234.75 (42.47)	1068.23 (235.51)	5000.60(1593.57)
P1,P4 - 90°	84.95 (16.19)	311.44 (48.98)	1102.91 (232.68)	5420.52 (1515.73)
P2,P3 - 90°	33.99 (4.54)	180.00 (34.80)	555.01 (106.15)	2437.18 (599.17)
P2,P4 - 90°	78.53 (16.16)	191.83 (31.51)	574.71 (106.74)	2508.57 (709.41)
P3,P4 - 90°	89.40 (17.77)	362.67 (61.17)	1329.94 (311.21)	6931.25 (1923.71)

Table 2

Velocity mean and standard deviation RMSE [m/s] per scenario (two planets observation).

Scenario	0.1 arcsec	1 arcsec	10 arcsec	100 arcsec
P1,P2 - 50°	0.026 (0.002)	0.049 (0.006)	0.143 (0.031)	0.659 (0.175)
P1,P3 - 50°	0.029 (0.002)	0.066 (0.014)	0.221 (0.050)	0.867 (0.303)
P1,P4 - 50°	0.040 (0.005)	0.089 (0.013)	0.224 (0.049)	0.980 (0.277)
P1,P3 - 90°	0.030 (0.002)	0.071 (0.013)	0.232 (0.050)	0.914 (0.283)
P1,P4 - 90°	0.039 (0.005)	0.091 (0.015)	0.241 (0.054)	0.100 (0.317)
P2,P3 - 90°	0.026 (0.002)	0.062 (0.010)	0.147 (0.0266)	0.459 (0.100)
P2,P4 - 90°	0.035 (0.005)	0.064 (0.010)	0.139 (0.027)	0.468 (0.119)
P3,P4 - 90°	0.041 (0.005)	0.101 (0.019)	0.271 (0.062)	1.345 (0.368)

estimation error decreases. However, before diving into the results, some clarifications are needed. While the definition of the steady-state for the fixed-geometry scenario is sufficiently straightforward, and with it the definition of convergence time, in a realistic scenario the definition of such is not unique. Fig. 10 reports the comparison between the ideal P2-P3 case, with the observation of Mars-Venus in three different time intervals. As the plot shows, the fixed-geometry case represents the asymptotic solution also in terms of convergence time. In fact, the best observation condition evolution (separation angle  $\beta = 90^\circ$ ) lays below the other three position error evolutions, that present an oscillatory behaviour as the observation condition varies through time. The observation condition also influences

the convergence time, as better measurements produce a quicker error decrease.

LoS measurement error has a significant influence on the convergence time, as reported in Table 3 for the single-planet case. For all the scenarios, it can be noticed a relevant increase in the convergence time with the increase of the error on the observations. As can be noticed in Fig. 8, the 3D-RMSE for the scenario P4 – 90° is in the same order of magnitude as the initial guess error, when  $\sigma_{los} = 100$  arcsec. So for this scenario, the computation of the convergence time is not applicable.

For the double-planets case, the convergence time results are shown in Table 4, where the same trend highlighted in the single-planet tracking scenario can be deduced. However, the observation of two planets generates a quicker convergence with respect to the single-planet tracking case.

The convergence time is also influenced by the tracking frequency. The results of the single-planet tracking scenario are reported in Table 5. For some cases, the drop in the convergence time with an increase in the tracking frequency is more evident, while in others the decrease in con-

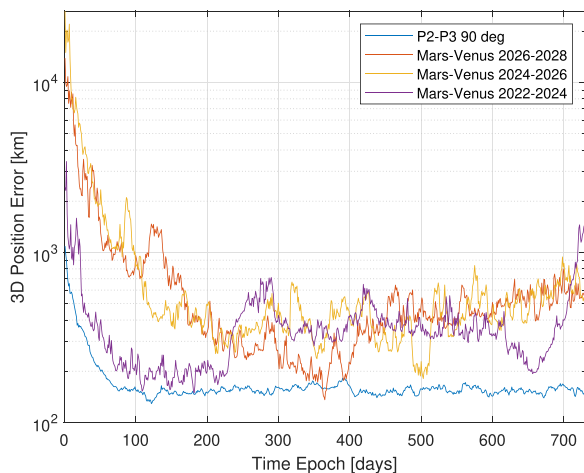


Fig. 10. Position error comparison between P2-P3 case, with  $\beta = 90^\circ$ , and the observation of the pair Mars-Venus in three time intervals.  $\sigma_{los} = 1$  arcsec.

Table 3

Convergence time [days] per scenario (one planet observation).

Scenario	0.1 arcsec	1 arcsec	10 arcsec	100 arcsec
P1 - 0°	162	185	283	521
P1 - 90°	154	235	375	636
P2 - 0°	174	197	243	418
P2 - 90°	160	217	405	539
P3 - 0°	163	198	370	551
P3 - 90°	228	281	477	617
P4 - 0°	188	283	521	628
P4 - 90°	447	532	638	N/A

Table 4  
Convergence time [days] per scenario (two planets observation).

Scenario	0.1 arcsec	1 arcsec	10 arcsec	100 arcsec
P1,P2 - 50°	31	89	271	457
P1,P3 - 50°	50	121	314	491
P1,P4 - 50°	44	196	321	566
P1,P3 - 90°	39	102	300	604
P1,P4 - 90°	44	168	295	562
P2,P3 - 90°	44	104	213	434
P2,P4 - 90°	95	144	233	428
P3,P4 - 90°	69	191	343	553

Table 5  
Convergence time [days] per scenario (one planet observation).

Scenario	0.5/day	1/day	2/day	4/day
P1 - 0°	202	185	175	141
P1 - 90°	244	235	170	167
P2 - 0°	198	197	176	133
P2 - 90°	276	217	186	175
P3 - 0°	230	198	167	142
P3 - 90°	346	281	245	216
P4 - 0°	376	283	221	191
P4 - 90°	588	532	478	444

vergence time is more modest. This shows that in general the geometry of the problem affects the convergence time, however, the general trend is that an increase in the tracking frequency generates a faster convergence to the steady-state. Moreover, it is important to highlight that in many scenarios doubling the tracking frequency results in a convergence time decreased by some tens of days. This is already an important result, as this information can drive the navigation strategy depending on the mission requirements.

Results for the double-planets observation scenario are reported in Table 6. First, the convergence to the steady-state is achieved more quickly, even with the lower tracking frequency, for which there is a convergence time lower than 230 days, while in the single-planet case it is often higher. The convergence time decreases by some tens of days when the tracking frequency is doubled, generating quicker convergence in all the test cases.

## 5. NEAs fly-by mission examples

This section is aimed to show the influence of a non-fixed geometry scenario, which has been briefly discussed

Table 6  
Convergence time [days] per scenario (two planets observation).

Scenario	0.5/day	1/day	2/day	4/day
P1,P2 - 50°	144	89	71	63
P1,P3 - 50°	168	121	75	59
P1,P4 - 50°	214	196	128	88
P1,P3 - 90°	188	102	91	61
P1,P4 - 90°	190	168	152	58
P2,P3 - 90°	132	104	57	50
P2,P4 - 90°	172	144	129	106
P3,P4 - 90°	226	191	147	96

in the introduction of the previous section. The test cases are two NEAs fly-by missions. The test cases have been defined with the help of the JPL Small-Body Mission-Design Tool (Roa et al., 2018), which allows the user to access a large dataset and to design missions towards NEA targets. A high-thrust (ballistic) scenario is considered. The tool solves Lambert's problem and provides the departure and arrival dates for ballistic transfer from the Earth to a certain NEA. However, it does not generate the trajectory, providing only the module of the excess velocity at departure, without directional information. So, the trajectory is here generated separately. The analysis is performed in an ECLIPJ2000 reference frame, centred in the Sun. Earth's heliocentric position is retrieved from Spice Toolkit (Acton, 1996; Acton et al., 2018) at the suggested departure date. The position of the target NEA at the arrival date is retrieved from the ephemerides generator of JPL Horizon (NASA-JPL, Accessed on 29th March 2022). Then, the ballistic trajectory is computed solving separately the Lambert's problem (Izzo, 2014). Once the departure velocity has been computed, the initial condition of the spacecraft is assumed to coincide with Earth's position at the departure time and with the computed velocity from Lambert's problem solution. The two asteroids that have been considered are 2008 UA202 and 2006 RH120, respectively the one with the lowest excess velocity and the one with the lowest relative velocity at the encounter, computed by the JPL Small-Body Mission-Design Tool.

The analysis presented in Section 4 is based on the strong assumption that planets are visible through the whole simulation time frame. This has been assumed to investigate the intrinsic properties of the method, but when realistic scenarios are analyzed, the planet's visibility needs to be considered. The planet is usually non-observable when the angle between the direction to it and the direction to the Sun, measured both from the spacecraft, is smaller than the Sun exclusion angle. Each hardware (camera or star-trackers), depending on its characteristics (especially depending on the baffle), has its Sun exclusion angle, and when the angle is lower, the instrument needs to be turned off because the sunlight can blind the sensor. For this analysis, a Sun exclusion angle of 30° has been chosen, according to star-trackers characteristics for CubeSat (Casini et al., 2021). This problem, as it is shown in the following test cases, especially refers to the observation of inner planets, which are also the best option for tracking to achieve lower error. So, a smart tracking strategy exploits the observation of inner bodies when possible, and switches to outer bodies when the former are not visible. This approach is used within the next test cases to define what planets to observe at each time epoch. Earth's observation is neglected in the next examples because the initial condition is considered coincident with the Earth's position, so the LoS direction measured in the first portion of the simulation is not completely realistic. In a more detailed mission scenario, the initial condition should be coincident with the exit from Earth's sphere-of-influence, but this is

far from the goal of this paper. In addition to that, the observability of the Earth in the first mission phases shall be analyzed according to hardware characteristics, as the planet disk may not fit the camera field-of-view, or may be too bright for the camera sensor (similar to the Sun). Moreover, as mentioned in Section 2, the trajectory generation is based on a higher-fidelity model. On the other hand, the filter's propagator is based on a 2-body dynamics, with the addition of planetary disturbances when their module overcomes a certain threshold. This leads to an extension of the previously defined  $\mathbf{F}$  matrix. For each planetary disturbance, the following matrix needs to be added to the lower-left  $3 \times 3$  partition of  $\mathbf{F}$ :

$$\tilde{\mathbf{F}}_k = \begin{bmatrix} -\mu_k \frac{\left(1 - 3\frac{x_{los,k}^2}{r_{los,k}^2}\right)}{r_{los,k}^3} & 3\mu_k \frac{x_{los,k}y_{los,k}}{r_{los,k}^3} & 3\mu_k \frac{x_{los,k}z_{los,k}}{r_{los,k}^3} \\ 3\mu_k \frac{x_{los,k}y_{los,k}}{r_{los,k}^3} & -\mu_k \frac{\left(1 - 3\frac{y_{los,k}^2}{r_{los,k}^2}\right)}{r_{los,k}^3} & 3\mu_k \frac{y_{los,k}z_{los,k}}{r_{los,k}^3} \\ 3\mu_k \frac{x_{los,k}z_{los,k}}{r_{los,k}^3} & 3\mu_k \frac{y_{los,k}z_{los,k}}{r_{los,k}^3} & -\mu_k \frac{\left(1 - 3\frac{z_{los,k}^2}{r_{los,k}^2}\right)}{r_{los,k}^3} \end{bmatrix} \quad (25)$$

The higher fidelity model used for the trajectory generation assumes a cannonball SRP model, whose general parameters have been defined in Section 2. For these test cases, a 3U CubeSat is considered, with  $m = 4$  kg, and  $A = 0.03$  m<sup>2</sup> (assuming the large side of the CubeSat is completely facing the Sun).

As remarked in Section 2.3, both light-time delay and velocity aberration are taken into account, following the procedure described in Mortari and Conway (2017).

Differently from the benchmark used in Section 4, the definition of steady-state behaviour is more complicated for a realistic mission scenario, as the changing geometry of the problem influences the behaviour of the estimation. In the next subsections, when the EKF provides low estimation error, it will be referred to as a ‘pseudo’ steady-state, meaning that the best estimation has been reached, but it is still subjected to small changes due to variations of the geometry. Alternatively, this can be interpreted as reaching a local steady-state solution for the given instant geometry.

Results of the Monte Carlo simulation are presented as the evolution through time of the average position error, for a fixed LoS error ( $\sigma_{LOS} = 1$  arcsec), and initial position and velocity error sampled respectively within  $10^5$  km and 0.1 km/s.

### 5.1. Test-case 1–2008 UA202

The trajectory generated by solving Lambert's problem is shown in Fig. 11. The departure and arrival dates are respectively 22–07–2028 and 20–10–2029, so the ToF corre-

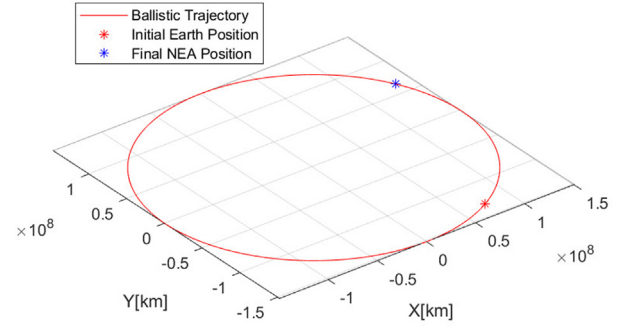


Fig. 11. Ballistic trajectory towards 2008 UA202.

sponds to 455 days. A full revolution around the Sun is needed to reach the target.

As already remarked, not all the planets are visible through the whole simulation time frame, because a certain Sun exclusion angle has to be guaranteed. Fig. 12 shows that only Mars is constantly visible through the whole simulation, so following the inner planet tracking strategy, before simulation date 110 and after 360 the observed pair is Venus-Mars, while in the middle is Mars-Jupiter.

The results of the simulation are reported in Fig. 13, where, for a fixed LoS error, the evolution of the position error is shown as a function of the simulation date for three tracking frequencies. On the other hand, the purple curve shows the evolution of the separation angle between the two observed planets. Discontinuities in the separation angle are due to changes in the observed pair of planets. The evolution of the position error can be described with the help of the results presented in Sections 3 and 4. Concerning geometry, small separation angles produce larger errors. This can be noticed in the proximity of simulation date 50. In the simulation interval between dates 270 and 360, an error increase can again be noticed. However, the error peak is not reached at the minimum separation angle. This is because this simulation interval is also characterized

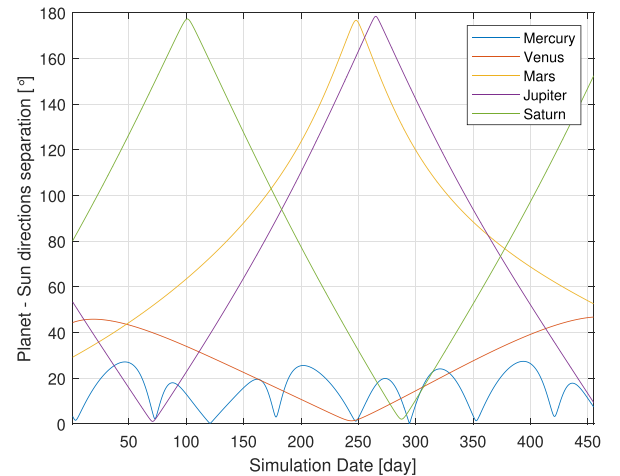


Fig. 12. Angular separation planet LoS and Sun direction in the simulation timeframe.



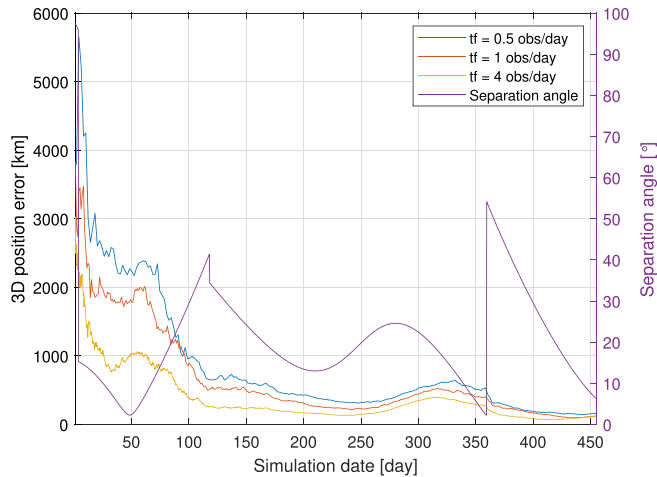


Fig. 13. 3D position error evolution in the simulation time-frame for three tracking frequencies, and the separation angle evolution.

by larger gravitational disturbances, that decrease around date 340. So the error around date 350 seems comparable to the error around date 300, despite a different separation angle. This test case is then useful also to highlight that the estimation error does not rely exclusively on the hardware characteristics, or observation strategy and geometry, but depends also on the actual dynamics and on the technique to account for gravitational disturbances in the navigation filter.

Moreover, it can be noticed that the observation of the pair Venus-Mars produces lower position error than the pair Mars-Jupiter, as predicted in Sections 3 and 4, and as it is evident in the error decrease after the simulation date 360. As already mentioned, it is difficult to define the steady-state behaviour for a geometry-changing simulation, however, it is evident how a higher tracking frequency let the position error decrease quicker (with a delay in the order of tens of days), however, when a pseudo steady-state solution is reached, the tracking frequency does not impact significantly the error, as remarked in Section 4, and as it can be noticed at the end of the simulation. Finally, the position error at the end of the simulation (so at the NEA approach), is  $\sim 200$  km, as expected from Section 4, where for the case P2-P3, with separation angle  $90^\circ$ , the RMSE was 180 km. Case P2-P3 is really similar to the observation Venus-Mars, and the larger error is due to a smaller separation angle. The error in the final phase of the simulation can be considered pseudo steady-state, and this is because the medium-large ToF gives sufficient time to the EKF to produce an accurate estimation of the state.

## 5.2. Test-case 2–2006 RH120

The trajectory to reach the NEA target is shown in Fig. 14. The departure and arrival dates are respectively 26–05–2028 and 04–11–2028, with  $\text{ToF} = 162$  days. This trajectory is shorter in time than the previous one, and a full revolution around the Sun is not achieved.

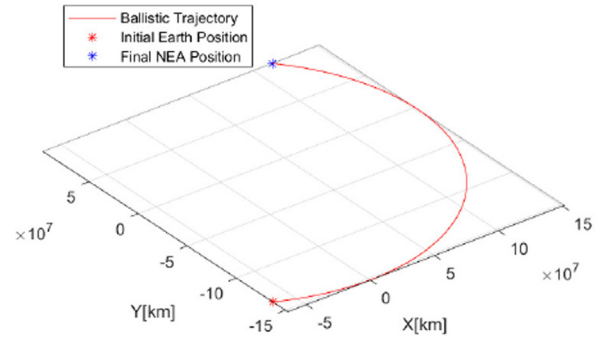


Fig. 14. Ballistic trajectory towards 2006 RH120.

Fig. 15 shows the angular separation of the planets, so following the same strategy, before simulation date 30 the observed pair is Jupiter-Saturn, after 30 and before 66 the observed pair is Mars-Jupiter, and then for the rest of the simulation, it is Venus-Mars. Similarly to the previous section, the results are presented in Fig. 16, where the position error evolution for different tracking frequencies can be observed.

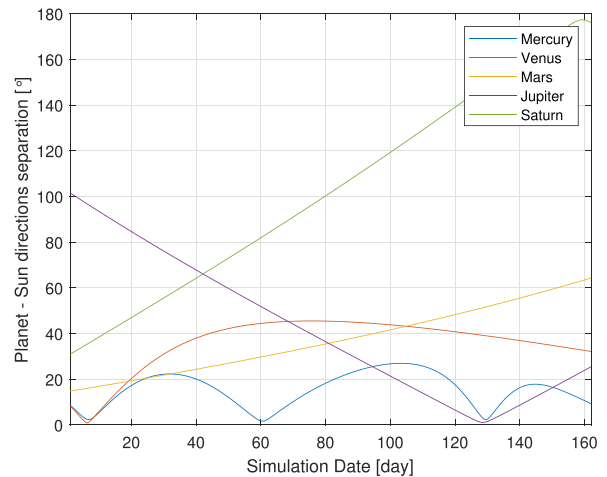


Fig. 15. Angular separation planet LoS and Sun direction in the simulation time frame.

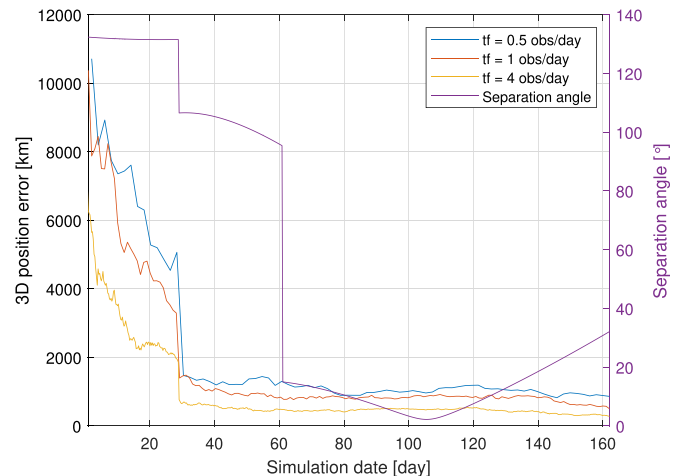


Fig. 16. 3D position error evolution in the simulation time-frame for three tracking frequencies, and the separation angle evolution.

Analogous conclusions on the separation angle can be highlighted. However, differently from the previous case, the effect of a higher tracking frequency on the position error is in the order of some hundreds of km, because for this shorter ToF the EKF does not reach a pseudo steady-state behaviour. This is also remarked by the error at the end of the simulation which oscillates between 500 and 1000 km (depending on the tracking frequency), which is larger than the error in the previous case, despite the same pair of planets being observed, even with a larger separation angle. This again shows how a higher tracking frequency is important to converge quickly to a better estimate, especially when the ToF is not sufficient to reach a pseudo steady-state behaviour. So, depending on the mission positioning requirements, it may be necessary either to increase the tracking frequency, or to improve the LoS measurement, either at software or hardware level.

## 6. Conclusions and remarks

The paper presents an analysis of the line-of-sight navigation technique for the state estimation of a deep-space cruising spacecraft. This work investigates the impact of both a hardware-driven parameter (LoS measurement error) and a navigation strategy parameter (tracking frequency) on both position/velocity RMSE and convergence time. At the same time, geometrical considerations are derived in a semi-analytical framework. The analysis is based on a set of planets, that rotate around the Sun with the same orbital speed as the simulated spacecraft. With this approach, the intrinsic impact of the relative geometry can be highlighted, having a simulation which is not scenario-dependent (specific spacecraft orbit, planets orbit, time-frame, etc.). The general results highlighted with this approach are then exploited in the description of two realistic NEA fly-by scenarios, showing how the considerations derived in a general framework relate to specific mission cases.

Concerning the geometry, the de-phasing angle analysis has shown a significant impact on the performance of the method. Tracking a planet that lies on the same radial vector as the spacecraft is beneficial to the performance. For the double-planets tracking case, also the separation angle plays an important role, as when it approaches  $90^\circ$ , the estimation error decreases.

Regarding the LoS measurement error, it largely influences both the performance of the method in terms of RMSE and convergence time. The RMSE does not scale down with the same factor as the observation error (which scales with a factor of 10 in this analysis), but still exponentially. The convergence time decrease is evident with more accurate observations, going below 100 days for the majority of the scenarios with  $\sigma_{los} = 0.1$  arcsec. Moreover, comparing the results of the single planet and the two planets tracking, it is evident that both position and velocity RMSE, and convergence time improve significantly with the observation of two planets rather than one. So again,

an autonomous LoS navigation system properly designed should always maximize the visibility window of at least two planets.

Convergence time is influenced by the tracking frequency, in fact, increasing the tracking frequency from one observation every two days to four observations per day produces a decrease in the convergence time of at least 50 days in most scenarios. Convergence times in the order of hundreds of days suggest that to achieve a small estimation error at the end of the cruise, LoS navigation should be performed during a large portion of the transfer, eventually increasing the tracking frequency when the spacecraft is approaching the target.

As shown in Section 5, considering the estimation error at the end of the trajectory, larger ToF allows for relaxation of requirements on LoS measurement error and tracking frequency, as the technique has ‘sufficient time’ to provide an accurate estimation, while for a smaller ToF a higher tracking frequency or a lower LoS measurement error are suggested to reduce the error.

These results demonstrate numerically that the current state-of-the-art for CubeSat technology is sufficiently accurate and precise to ensure the applicability of LoS navigation to deep-space cruising, as for  $\sigma_{los}$  in the range 10–100 arcsec, the position RMSE spans from some hundreds of km to few thousands of km in most scenarios, with an evident performance improvement in the two planets tracking case. These values are acceptable for many mission scenarios involving CubeSat cruising in deep-space, as these position errors allow trajectory correction manoeuvres achievable with micro-propulsion system technology (Casini et al., 2021; Walker et al., 2021). Moreover, the achievable navigation error is comparable to that of the CubeSat INSPIRE, whose estimated navigation error is  $\sim 500$  km relatively close to the Earth, and  $\sim 1000$ – $2000$  km further away, using the Iris X-band transponder (Klesh et al., 2013).

However, if the space application requires lower error, achieving  $\sigma_{los} = 0.1$  arcsec would be particularly interesting to reduce drastically the RMSE, having an accurate autonomous navigation system in deep-space, but also to give more flexibility to the navigation strategy design, as it would allow quicker convergence. Increasing the tracking frequency allows quicker convergence, but needs to comply with operations and power requirements.

LoS navigation is viable for deep-space applications requiring higher autonomy, and it is exploitable by the next-generation deep-space CubeSat, whose navigation strategy design can be driven by the results presented in this paper.

## Declaration of Competing Interest

The authors declare that they have no known competing financial interests or personal relationships that could have appeared to influence the work reported in this paper.

## Acknowledgments

This research was funded by the EU H2020 MSCA ITN Stardust-R, grant agreement 813644 (DOI <https://doi.org/10.3030/813644>).

## References

- Acton, C., 1996. Ancillary data services of NASA's navigation and ancillary information facility. *Planet. Space Sci.* 44 (1), 65–70.
- Acton, C., Bachman, N., Semenov, B., Wright, E., 2018. A look towards the future in the handling of space science mission geometry. *Planet. Space Sci.* 150 (1), 9–12.
- Andreis, E., Franzese, V., Topputo, F., 2022. Onboard orbit determination for deep-space cubesats. *J. Guid. Control Dyn.* 45 (8), 1466–1480.
- Carpenter, J., D'Souza, C., 2018. Navigation filter best practices. Technical report NASA/TP-2018-219822.
- Casini, S., Fodde, I., Monna, B., Cervone, A., Gill, E., 2021. Novel 3U stand-alone cubesat architecture for autonomous near Earth asteroid fly-by. *Aerospace* 8 (9).
- Dahir, A., Kubitschek, D., Palo, S., 2019. Recovering time and state for small satellites in deep space. In: Proc. of the 33th Small Satellite Conference, Logan (UT) SSC19-WKIV-04.
- Enright, J., Jovanovic, I., Kazemi, L., Zhang, H., Dzamba, T., 2018. Autonomous optical navigation using nanosatellite-class instruments: a Mars approach case study. *Celest. Mech. Dyn. Astron.* 130 (13).
- Franzese, V., Di Lizia, P., Topputo, F., 2018. Autonomous optical navigation for LUMIO mission. In: Proc. of the SCITECH Space Flight Mechanics Meeting, Kissimmee (FL). AIAA 2018-1977.
- Franzese, V., Topputo, F., 2019. Line-of-sight deep-space autonomous navigation. *arXiv:1909.08459*.
- Franzese, V., Topputo, F., 2020. Optimal beacons selection for deep-space optical navigation. *J. Astronaut. Sci.* 67, 1775–1792.
- Franzese, V., Topputo, F., Ankersen, F., Walker, R., 2021. Deep-space optical navigation for M-ARGO mission. *J. Astronaut. Sci.* 68, 1034–1055.
- Frauenholz, R.B., Bhat, R.S., Chesley, S.R., Mastrodemos, N., Owen, W. M., Ryne, M.S., 2008. Deep impact navigation system performance. *J. Spacecr. Rockets* 45 (1), 39–56. <https://doi.org/10.2514/1.24310>.
- Izzo, D., 2014. Revisiting Lambert's problem. *Celest. Mech. Dyn. Astron.* 121, 1–15.
- Jean, I., Ng, A., Misra, A., 2019. Impact of solar radiation pressure modeling on orbital dynamics in the vicinity of binary asteroids. *Acta Astronaut.* 165, 167–183.
- Karimi, R., Mortari, D., 2015. Interplanetary autonomous navigation using visible planets. *J. Guid. Navig. Control* 38 (6).
- Klesh, A., Baker, J., Castillo-Rogez, J., Halatek, L., Murphy, N., Raymond, C., Sherwood, B., Bellardo, J., Cutler, G., Lightsey, J., 2013. INSPIRE: Interplanetary nanospacecraft pathfinder in relevant environment. In: Proc. of the 27th Small Satellite Conference, Logan (UT) SSC13-XI-8.
- Ma, X., Chen, X., Fang, J., Liu, G., Ning, X., 2016. Observability analysis of autonomous navigation for deep space exploration with LOS/TOA/velocity measurements. In: Proc. of the IEEE Aerospace Conference, Big Sky (MT), pp. 1–9. doi:10.1109/AERO.2016.7500663.
- Machuca, P., Sanchez, J., Greenland, S., 2019. Asteroid flyby opportunities using semi-autonomous cubesats: Mission design and science opportunities. *Planet. Space Sci.* 165, 179–193.
- Marini, A., Lumb, R., Racca, G., Foing, B., Almeida, M., 2002. Technology and science from Earth to Moon: SMART-1 experiments and their operations. In: Proc. of the 36th ESLAB Symposium, Noordwijk (NL), pp. 95–100.
- Mortari, D., Conway, D., 2017. Single-point position estimation in interplanetary trajectories using star trackers. *Celest. Mech. Dyn. Astron.* 128, 115–130.
- NASA-JPL, Accessed on 29th March 2022. Horizons system. <https://ssd.jpl.nasa.gov/horizons/app.html#/>.
- Pellacani, A., Graziano, M., Fittock, M., Gil, J., Carnellu, I., 2019. HERA vision based gnc and autonomy. In: Proc. of the 8th European Conference for Aeronautics and Space Sciences (EUCASS), Madrid (Spain), pp. 1–14.
- Roa, J., Chamberlin, A., Park, R., Petropoulos, A., Chodas, P., Landau, D., Farnocchia, D., 2018. Automatic design of missions to small bodies. In: Proc. of the SCITECH Space Flight Mechanics Meeting, Kissimmee (FL). AIAA 2018-0200.
- Tapley, B., Schutz, B., Born, G., 2004. Chapter 4 - fundamentals of orbit determination. In: Elsevier (Ed.), *Statistical Orbit Determination*. Academic Press, Burlington, pp. 159–284. <https://doi.org/10.1016/B978-012683630-1/50023-0>, URL: <https://www.sciencedirect.com/science/article/pii/B9780126836301500230>.
- Turan, E., Speretta, S., Gill, E., 2022a. Autonomous navigation for deep space small satellites: scientific and technological advances. *Acta Astronaut.* 193, 56–74. <https://doi.org/10.1016/j.actaastro.2021.12.030>, URL: <https://www.sciencedirect.com/science/article/pii/S0094576521006652>.
- Turan, E., Speretta, S., Gill, E., 2022b. Performance analysis of crosslink radiometric measurement based autonomous orbit determination for cislunar small satellite formations. *Adv. Space Res.* <https://doi.org/10.1016/j.asr.2022.11.032>, URL: <https://www.sciencedirect.com/science/article/pii/S0273117722010638>.
- Vasile, M., Sironi, F., Bernelli-Zazzera, F., 2002. Deep space autonomous orbit determination using CCD. In: Proc. AIAA/AAS Astrodynamics Specialist Conference and Exhibit, Monterey (CA).
- Walker, L., Di Carlo, M., Greco, C., Vasile, M., Warden, M., 2021. A mission concept for the low-cost large-scale exploration and characterisation of near earth objects. *Adv. Space Res.* 67 (11), 3880–3908.